
PERGAMON

Journal of the Mechanics and Physics of Solids
49 (2001) 2071–2093

JOURNAL OF THE
MECHANICS AND
PHYSICS OF SOLIDS

www.elsevier.com/locate/jmps

Optimal design of a flexural actuator

T.J. Lu[a,b], J.W. Hutchinson[c], A.G. Evans[b,*]

[a] *Department of Engineering, University of Cambridge, Trumpington Street, Cambridge CB2 1PZ, UK*
[b] *Materials Institute, Princeton University, 70 Prospect Avenue, Princeton, NJ 085404-5263, USA*
[c] *Division of Engineering and Applied Science, Harvard University, Cambridge, MA 02138, USA*

Abstract

A minimum-weight flexural actuator is designed. The actuator comprises a triangular corrugated core with shape memory alloy (SMA) faces. It is clamped at one end and free at the other. For design and optimization, the temperature history of the face sheets upon heating and subsequent cooling is first obtained as a function of the cooling efficiency (Biot number) and the operational frequency deduced. Based upon this response, a phenomenological model is employed to represent the martensite evolution. Thereafter, the end deflection is calculated as a function of temperature. The minimum weight is calculated subject to the provisos that: (i) the end deflection attains a specified value; (ii) the power consumed is less than the upper limit of the supply; and failure is averted by (iii) face/core yielding and (iv) face/core buckling; (v) the operational frequency of the panel achieves a specified limit.

Keywords: A. Microstructures; Phase transformation; Thermomechanical processes; B. Sensors and actuators; C. Optimization

1. Introduction

Actuators embrace a size range from nanometers to meters, with electrical, magnetic, thermal or pneumatic input signals (Ataka et al., 1993; Lin and Lin, 1998). Shape memory alloy (SMA) actuators are the subject of this study. They use a thermal input signal to generate motion. Such actuation is relatively simple (no sliding seal or liquid encapsulation), yet enables three-dimensional linear or rotary motion, such as maneuverable underwater vehicles (Webb et al., 2000). The present objective is to design and analyze lightweight flexural actuators that realize large bending displacements against a restraining moment, within an allowable power budget. Guidelines from ultra-light

* Corresponding author. Tel.: +1-609-975-4762; fax: +1-609-975-1177.
E-mail address: anevans@princeton.edu (A.G. Evans).

0022-5096/01/$ - see front matter
PII: S0022-5096(01)00024-2

materials and structures (Budiansky, 1999; Wicks and Hutchinson, 2000) are used to select appropriate topologies.

Beams with corrugated cores have been chosen as the basic topology. Corrugated panels have been widely used in civil and military applications, owing to excellent specific stiffness and strength. Examples include metallic panels for aerospace and naval applications (Allen, 1969; Wiernicki et al., 1991; Jegley, 1992) as well as fiber boards (Lu et al., 2001). Such panels become attractive when all performance characteristics (fabrication, installation, assembly and costs) are considered, on a total system basis (Wiernicki et al., 1991; Jegley, 1992). To our knowledge, there have been no attempts at using such designs for actuators.

The analysis will focus on NiTi-based SMAs (tradename Nitinol). This SMA is austenitic at relatively high temperatures, but converts to twinned martensite upon cooling. The temperature range over which the shape memory effect takes place in NiTi alloys is 50–70°C. The stress/strain curve for the martensite exhibits a stress plateau as its variants align with the load axis. The material completely recovers its shape upon heating when the de-twinned martensite transforms back to austenite. A two-way shape memory effect is also possible, wherein the alloy repeatedly recalls its deformed and undeformed shapes upon cooling and heating. It is created upon repetitive thermo-mechanical *training* (Zhang et al., 1997; Kato et al., 1998; Otsuka and Wayman, 1998), which introduces a residual stress that enables only a single variant to form upon cooling. A trained SMA exhibits up to 5% recoverable strain (Otsuka and Wayman, 1998).

The article is organized in the following manner. The lightweight actuator concept is presented and the associated design problem stated. The complete temperature history of the SMA face sheets upon heating and cooling is obtained. An analysis is then performed to find the minimum weight that achieves (i) a specified displacement, subject to (ii) a restraining moment, that (iii) assures no failure, and (iv) operates within a power budget.

2. The actuator design

2.1. The concept

We contemplate a lightweight beam (Fig. 1) which must flex over a displacement δ_0 (Fig. 1c) against restraining springs and dashpots (Fig. 1a). The restraint is modeled here as a constant force, N (Fig. 1b). A subsequent analysis will allow the force to vary with displacement and frequency. The face sheets are made from SMA, actuated by resistive (Joule) heating. Two types of core material are selected. (a) For actuators with dimensions in the centimeter-to-meter range, the core comprises a corrugated polymer, which is thermally and electrically insulating. The apex of each corrugation has a small attachment pad made of the same polymer to facilitate bonding (Fig. 1). (b) For micro-scale devices (e.g., MEMs), Si is chosen as the core, with a silica layer used for thermal and electrical insulation.

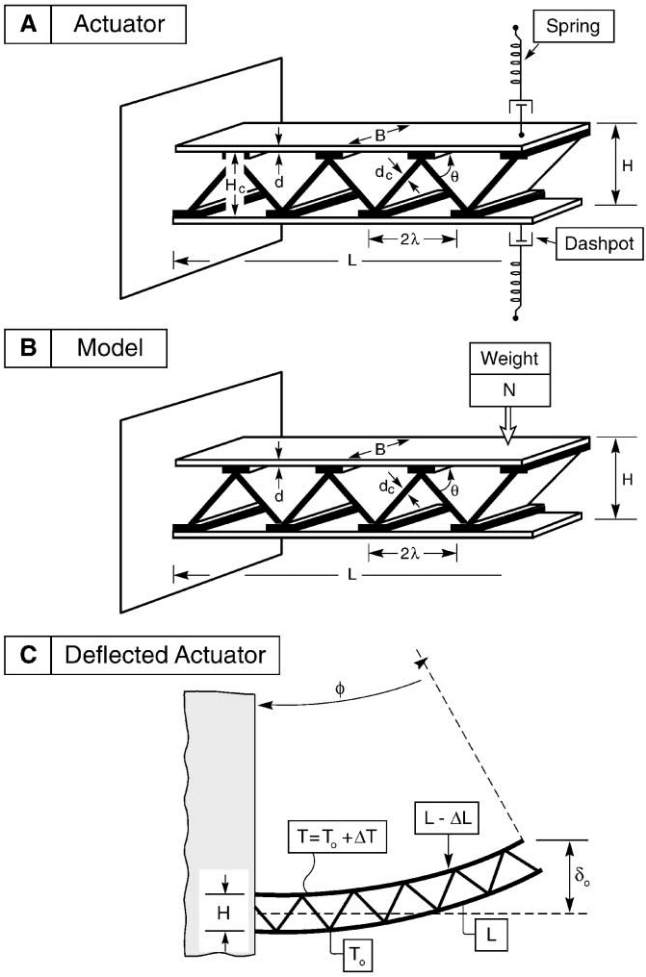

Fig. 1. Geometry and conventions for cantilever beam with triangular corrugated core: (a) actuator design; (b) the model and (c) deflection of beam when its top face is actuated.

A triangular corrugation has been chosen for the core because of the following dual attributes that appear not to have been previously exploited in actuator design.

(i) It offers no rotational resistance when comprised of frictionless-pinned joints. Moreover, it provides negligible resistance to the stretching and contraction of the SMA face sheets as they actuate. That is, for a well-designed joint, the localized flexural stresses in the core are small compared with the uniform axial stresses. *Accordingly, as one of the face sheets contracts to induce bending, the core remains essentially unstressed and does not store elastic energy.*

(ii) When attached to the face sheets, the triangulated configuration has exceptional bending stiffness that inhibits the counter deflection induced by the imposed forces and

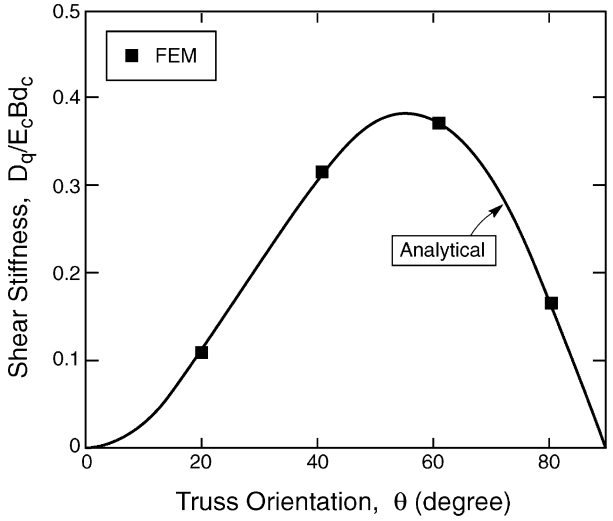

Fig. 2. Non-dimensional transverse shear stiffness of corrugated panel as function of corrugation angle.

moments. The bending stiffness arises because core shear is dominated by stretching and contraction of the members (no bending). An analytical result for the transverse shear stiffness (based on stretching) is

$$D_q = E_c B d_c \sin^2\theta\cos\theta, \tag{1}$$

wherein the core has thickness d_c, height H_c, pitch length 2λ, corrugation angle, $\theta = \tan^{-1}(H_c/\lambda)$, (Fig. 1). Selected finite element calculations made using Timoshenko beam elements affirm that (1) is an excellent representation (Fig. 2). Note that this stiffness is maximized at, $\theta = \tan^{-1}(\sqrt{2}) = 54.7^\circ$ (or, equivalently, $H = \sqrt{2}\lambda$).

2.2. Problem definition

The following cycle is envisaged. The top SMA face sheet is heated to temperature, $T(=T_0+\Delta T)$, by transmitting an electrical current, while the bottom face sheet and the core are maintained below the martensite finish temperature, T_{Mf}. At the end of heating, the peak temperature of the top face T_f is higher than the finish temperature for the austenite transformation, T_{Af}, and the corresponding tip deflection reaches its maximum, δ_f (Fig. 1c). Cooling is initiated as soon as T_f is reached. As $T \to T_0$, the cantilever recovers its original configuration ($\delta = 0$). Identical face sheets made of a two-way SMA are assumed: a related analysis applies to a one-way material. Unless otherwise stated, the properties of the face sheet and core materials are taken to be temperature independent.

The actuator has non-dimensional weight

$$W/\rho_f BL^2 = 2d/L + (\rho_c/\rho_f)d_c/L\cos\theta. \tag{2}$$

The aim is to find the lowest W. The design problem addresses temperatures, power requirements, failure mechanisms and displacements.

The following definitions are used. The SMA has thickness, d, density, ρ_f, recoverable strain, ε_T, thermal expansion coefficient, α_f, thermal conductivity, k_f, thermal diffusivity, κ_f, electrical resistance, R ($\equiv \sigma_\rho L/Bd$, with σ_ρ being the electrical resistivity), specific heat, c_p^f, Young's modulus, E_f (E_M for martensite, and E_A for austenite, with $E_A \approx 3E_M$) and yield strength, σ_Y^f. It is assumed that the face sheet and core have identical Poisson ratio, ($v_f = v_c = v$, $v = 1/3$). It is further assumed that $H_c/d_c \gg 1$, $H_c/d \gg 1$, $\lambda/d_c \gg 1$, and $\lambda/d \gg 1$; that is, $H_c \cong H$.

3. Design problem

3.1. Temperature history

3.1.1. General case

The SMA is actuated by resistive heating the face sheet with an electric current, I. The power supplied to the actuator is

$$P = I^2 R, \tag{3}$$

where P is in watts (W), I in amperes (A) and R in ohms (Ω). The power is converted into heat in a spatially uniform manner and is consumed by three mechanisms: (i) temperature increase of the face sheet relative to the initial temperature; (ii) convective heat transfer (radiative heat transfer is negligible); (iii) phase transformation. Since the polymer and silica both have thermal conductivity, k_c, at least an order of magnitude smaller than that for SMA ($\sim$ 20W/m K, Peirs et al., 1998), conduction loss across the core is neglected. (This is an oversimplification for Si cores, since Si itself has high k_c.) Under these assumptions, the temperature variation of the face sheet with respect to time and position is as follows (Carslaw and Jaeger, 1959). For heating ($t \leqslant t^+$):

$$\rho_f c_p^f \frac{\partial T}{\partial t} = k_f \frac{\partial^2 T}{\partial x^2} - \frac{2h}{d}(T - T_0) + \sigma_\rho \left(\frac{I}{Bd}\right)^2 + \frac{\rho_f BLd\Theta}{\Delta t}, \tag{4}$$

where Θ denotes the latent heat, t^+ signifies the end of heating as well as the beginning of cooling (Fig. 3), Δt represents the duration of phase change, and h is the surface heat transfer coefficient. Based on the geometrical and material parameters for TiNi alloys (Table 1), the (third) term in Eq. (4) governed by Joule heating is at least an order of magnitude larger than the (fourth) term due to phase change. Moreover, experimentally it has been found that the effect of latent heat on the cycle time is small ($<10\%$) (Makino et al., 2000; Webb et al., 2000). Accordingly, for simplicity, the effect of phase change on the temperature history will be neglected, whereupon Eq. (4) simplifies to

$$\rho_f c_p^f \frac{\partial T}{\partial t} = k_f \frac{\partial^2 T}{\partial x^2} - \frac{2h}{d}(T - T_0) + \sigma_\rho \left(\frac{I}{Bd}\right)^2. \tag{5}$$

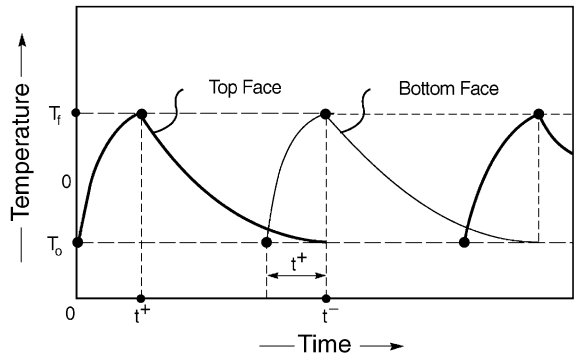

Fig. 3. Schematic of heating and cooling curves of top and bottom faces during one full cycle.

Note that, in general, the electrical resistivity σ_ρ varies with temperature, and exhibits hysteresis (Otsuka and Wayman, 1998; Makino et al., 2000). For simplicity, it is taken as the average over the full temperature cycle. In order to obtain a solution to Eq. (5), two generic boundary conditions are considered. (a) Type I, wherein both ends of the cantilever remain at ambient, because of heat conduction through attachments. (b) Type II wherein only the attached end is at ambient: the free end being thermally insulated. For type I, the conditions upon heating are

$$T(x,0) = T_0, \tag{6}$$

$$T(0,t) = T_0 \quad \text{and} \quad T(L,t) = T_0. \tag{7}$$

The solution is given by (Carslaw and Jaeger, 1959)

$$\frac{T(x,t)}{T_0} = 1 + \frac{2\bar{P}}{\pi}\sum_{m=1}^{\infty}\frac{\mu^2}{(2m-1)[(2m-1)^2\pi^2+\mu^2]}\sin\frac{(2m-1)\pi x}{L} \times\{1-\mathrm{e}^{-[\mu^2+(2m-1)^2\pi^2](d/L)^2\bar{t}}\}, \tag{8}$$

where the non-dimensional parameters are: $\bar{P} = P/BLhT_0$ ($\equiv \sigma_\rho I^2/B^2\,dhT_0$), $\bar{t} = \kappa_f t/d^2$, $\mu = (L/d)\sqrt{2Bi}$, with $Bi \equiv hd/k_f$ the Biot number. Note that the expression for the steady-state temperature of the SMA ($t \to \infty$) can be simplified, because

$$\frac{2}{\pi}\sum_{m=1}^{\infty}\frac{\mu^2}{(2m-1)[(2m-1)^2\pi^2+\mu^2]}\sin\frac{(2m-1)\pi x}{L} = \frac{1}{2}\left[1-\frac{\sinh\mu x/L+\sinh\mu(1-x/L)}{\sinh\mu}\right].$$

At $t = t^+$, when the top face sheet reaches T_f, the electrical current is switched off and cooling begins.

Table 1
Parameters used in illustrations

Thickness, $d = 0.5\,\text{mm}$
Width, $B = 1\,\text{cm}$
Length, $L = 0.1\,\text{m}$
Density, $\rho_f = 6500\,\text{kg/m}^3$
Specific heat, $c_p^f = 500\,\text{J/kg}$
Latent heat, $\theta = 10,000\,\text{J/kg}$
Heat transfer coefficient (natural convection) $h = 50\,\text{W/m}^2\text{K}$

The corresponding equation for cooling is ($t \geqslant t^+$):

$$\rho_f c_p^f \frac{\partial T}{\partial t} = k_f \frac{\partial^2 T}{\partial x^2} - \frac{2h}{d}(T - T_0) \tag{9}$$

and the initial and boundary conditions are

$$T(x, t^+) = T_f(x, t^+), \tag{10a}$$

$$T(0, t) = T_0 \quad \text{and} \quad T(L, t) = T_0. \tag{10b}$$

The solution is given by

$$\frac{T(x,t)}{T_0} = 1 + \frac{2\bar{P}}{\pi} \sum_{m=1}^{\infty} \frac{\mu^2}{(2m-1)[(2m-1)^2\pi^2 + \mu^2]} \sin\frac{(2m-1)\pi x}{L} \times \{e^{-[\mu^2+(2m-1)^2\pi^2](d/L)^2(\bar{t}-\bar{t}^+)} - e^{-[\mu^2+(2m-1)^2\pi^2](d/L)^2\bar{t}}\}. \tag{11}$$

For type II boundary conditions

$$T(0, t) = T_0 \quad \text{and} \quad dT(L, t)/dt = 0.$$

Solutions (8) and (11) still hold, except that L should be replaced by $2L$.

For illustration, consider a Nitinol sheet having the characteristics indicated in Table 1,

and let the electrical current $I = 20\,\text{A}$. The corresponding value of μ is 10. For the type I boundary condition, the temperature is largely uniform at all times except near the ends (Fig. 4a). However, if L is reduced to 1 cm (with the remaining parameters unchanged), such that $\mu = 1$, the temperatures are much less uniform (Fig. 4b). Also, for the same power ($\bar{P} = 8$), the peak temperature achieved as $\bar{t} \to \infty$ is significantly lower. Similar trends are observed in Fig. 5 for type II boundary conditions.

3.1.2. Thin SMA faces

For thin faces, the variation of temperature along the length may be neglected. Then the solution becomes ($t \leqslant t^+$):

$$T(t) = T_0 + \frac{I^2 R}{2BLh}(1 - e^{-t/\tau}), \tag{12a}$$

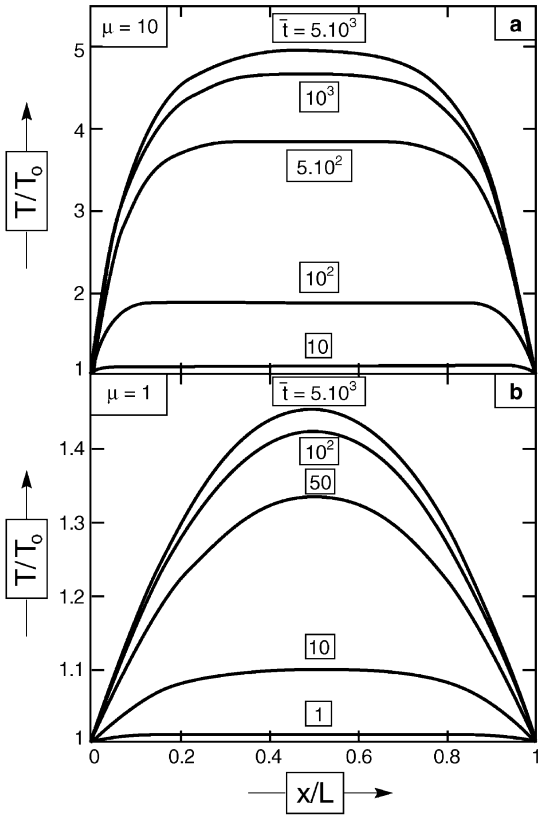

Fig. 4. Transient temperature distribution of face for type I boundary conditions: (a) $\mu = 10$; (b) $\mu = 1$. The rest of parameters are listed in Table 1.

where the thermal time constant is

$$\tau \equiv \frac{\rho_{\mathrm{f}} c_p^{\mathrm{f}} d}{2h}. \tag{12b}$$

Consider a Nitinol sheet (Table 1) wherein the temperature is required to increase by, $\Delta T_{\mathrm{f}} = 50^{\circ}\mathrm{C}$, in time t. The corresponding current must satisfy

$$I \geqslant 5/\sqrt{1 - \mathrm{e}^{-t/16.25}}. \tag{13}$$

For example, specifying a rise time of 1 s, the current needed is, $I \geqslant 20\,\mathrm{A}$. The associated ramp-up time t^{+} is

$$\frac{t^{+}}{\tau} = -\ln\left(1 - \frac{\Delta T_{\mathrm{f}}}{P/2BLh}\right). \tag{14}$$

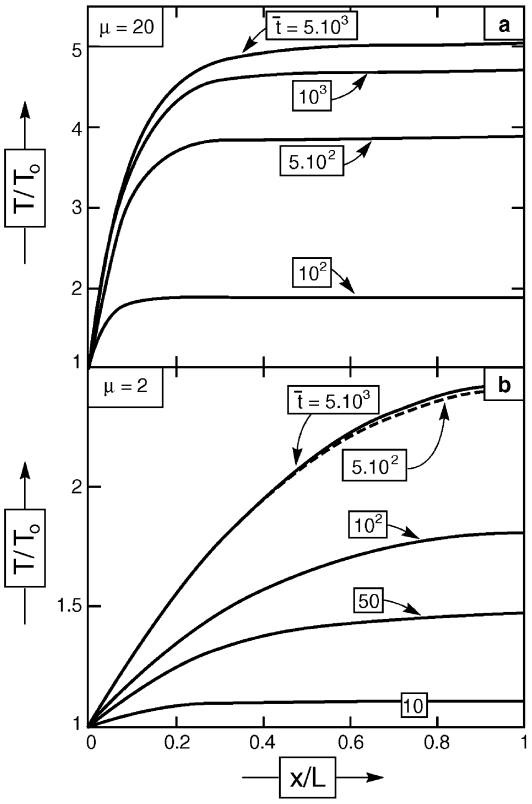

Fig. 5. Transient temperature distribution of face for type II boundary conditions: (a) $\mu = 20$; (b) $\mu = 2$. The rest of parameters are listed in Table 1.

The evolution of the top surface temperature is ($t \geqslant t^+$):

$$T = T_0 + \Delta T_f e^{-(t-t^+)/\tau}. \tag{15}$$

The temperature variation with time, as well as the associated tip deflection, are illustrated on Fig. 6. During heating, the cantilever initially deflects downwards ($T < T_{As}$) as a result of thermal expansion. Beyond T_{As}, the cantilever starts to bend upwards as the shape memory contraction overcomes thermal expansion (reaching $\delta = \delta_f$ when the transformation finishes at $T = T_{Af}$). Further temperature increase beyond T_{Af} would cause the tip deflection to *decrease* because of thermal expansion. As soon as cooling starts, at $T = T_f$, the tip deflection decreases, initially due to relaxation of thermal expansion, subsequently assisted by the commencement of the martensite transformation. Because this transformation is exothermic (Makino et al., 2000), there is a brief stagnation at $T = T_{Ms}$.

In general, the tip deflection increases with increasing heating rate. This happens because the temperature distribution in the face sheet becomes more uniform as the

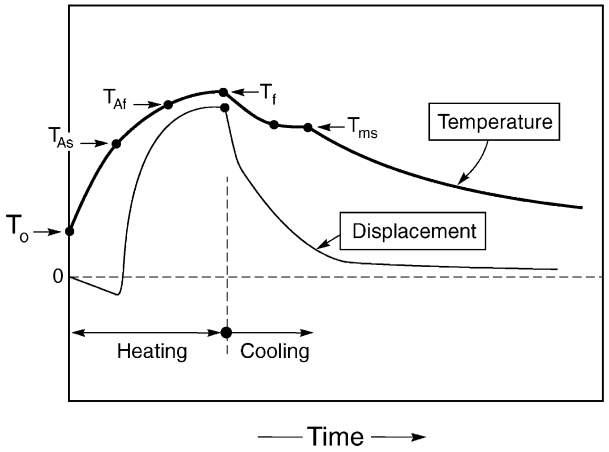

Fig. 6. Schematic of face temperature and tip deflection with time.

rate of heating is increased (less time for heat dissipation into the ambient), so that shape change occurs nearly everywhere in the face before cooling begins. This effect is more pronounced for relatively short cantilevers. From Eq. (12a), the rate of heating is obtained as

$$\frac{\mathrm{d}T}{\mathrm{d}t} = \frac{P}{\rho_{\mathrm{f}} c_p^{\mathrm{f}} BLd} \mathrm{e}^{-t/\tau}. \tag{16}$$

It is increased by increasing the power, P, by decreasing either the heat transfer coefficient or the face sheet thickness. However, a small h slows down the rate of cooling and reduces the operational frequency, and moreover, a thin face sheet encourages yielding and buckling.

3.2. Operational frequency

As a practical matter, cooling is considered to finish when $(T - T_0)/\Delta T_{\mathrm{f}} = 0.05$ (or, $\delta/\delta_{\mathrm{f}} = 0.05$). The corresponding time at the end of cooling is therefore

$$t^- = t^+ + 3\tau. \tag{17}$$

Using the parameters for a NiTi sheet (Table 1) with $I = 20\,\mathrm{A}$, then $t^+ = 1\,\mathrm{s}$ and $t^- = 50\,\mathrm{s}$. That is, the operational frequency of the actuator would be about 0.02 Hz, if only the top face sheet were actuated. The frequency can be somewhat increased if the top and bottom face sheets are alternatively actuated (Fig. 3), whereupon the time scale is, $t_0 \equiv 2t^- - t^+$, and the operational frequency becomes

$$f \equiv \frac{1}{t_0} = \frac{2h}{\rho_{\mathrm{f}} c_p^{\mathrm{f}} d} \left\{ 6 - \ln\left(1 - \frac{2BLh\Delta T_{\mathrm{f}}}{P} \right) \right\}^{-1}. \tag{18}$$

The operational frequency is largely limited by the efficiency of cooling. This frequency can be increased by reducing the face thickness, d, or by increasing the heat transfer

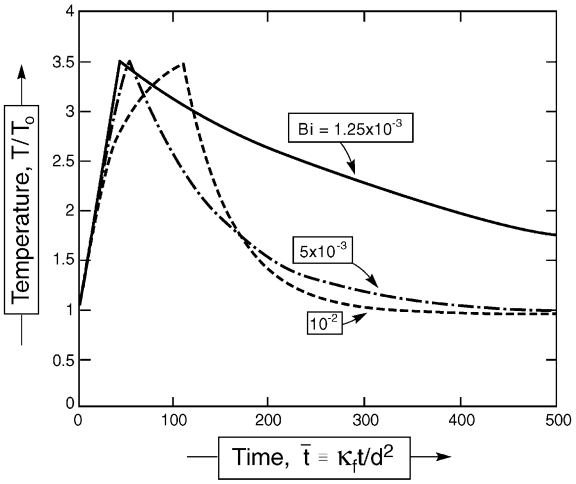

Fig. 7. Surface temperature versus time curve for selected values of Biot number $Bi = hd/k_f$. The parameters of Table 1 are used for plotting.

coefficient, h. For thin film SMA faces, the rapid heat transfer due to small thermal mass and large surface area to volume ratios implies that a frequency in the 100 Hz range is achievable (Krulevitch et al., 1996). However, d cannot be arbitrarily reduced as this would cause yielding and buckling of the face. The heat transfer coefficient can be increased by using forced convection or liquids in the cooling half-cycle (Lu, 1999; Gu et al., 2001). For example, in underwater applications, an actuation frequency up to 2 Hz has been achieved (Webb et al., 2000).

For the parameters in Table 1 and $I = 50$ A, Fig. 7 plots the predicted heating–cooling curve of the top face for $h = 50$, 200, 400 W/m^{2}K, respectively. Note that h has a relatively small influence on the face heating, but substantially affects its cooling and hence, the operational frequency.

In practice, Eqs. (12b), (14) and (16) can be used to calibrate the two parameters of greatest uncertainty: h and k_f. That is, the surface temperature as a function of time may be used to calculate τ from Eq. (16). The heat transfer coefficient is subsequently obtained by substituting τ into Eq. (14). Finally, k_f is obtained from τ and h by using Eq. (12b).

3.3. Electro-mechanical power consumption

Within a full thermal cycle (both faces actuated), the heat needed to raise the temperature of the faces to drive the structure is

$$Q_f = \frac{\rho_f c_p^f \, dP}{h} \int_{T_0}^{T_f} dT = 2P\tau(1 - e^{-t^+/\tau}). \tag{19}$$

The loss of heat due to surface convection during the cycle is

$$Q_c = Q - Q_f, \tag{20}$$

where $Q = 2Pt^+$ is the total energy input per cycle.

If the power supply has a specified upper limit, P_0, then the design of the actuator is subject to the constraint that

$$P \leqslant P_0 \tag{21}$$

which, in view of Eq. (14), can be rewritten as

$$2BLh\Delta T_f(1 - e^{-2ht^+/\rho_f c_p^f d})^{-1} \leqslant P_0. \tag{22}$$

Note that, in addition to material and geometrical parameters, the ramp-up time t^+ (the time that the power remains on) is important.

3.4. Member stresses

Stresses are induced in the members by the resistive load, N (Fig. 1b). The stresses in the faces are proportional to the global moment, whereas the stress in the core is proportional to the global shear force. The maximum stress induced in the face occurs at the clamped end which, with the assumption that $H/L \ll 1$, is obtained from equilibrium considerations as

$$\sigma_f = \pm \frac{N}{Bd}\frac{L}{H}, \tag{23}$$

where "+" stands for the top face and "−" for the bottom. The stresses experienced by the members of the triangular core are

$$\sigma_c = \frac{N}{Bd_c \sin\theta} \tag{24}$$

which alternates from tension in one member to compression in its immediate neighbors.

3.5. Phase transformation strain

Upon heating, the strain experienced by the face ε_f is the sum of three contributions: (a) elastic strain due to stress σ_f, (b) thermal expansion, and (c) phase transformation, such that

$$\varepsilon_f(T) = \sigma_f/E_f(T) + \alpha_f(T - T_0) - \varepsilon_T[(1 - \zeta^+(T))], \tag{25a}$$

where ζ^+ is the fraction of the martensite phase during heating, with $\zeta^+ = 1$ for $T \leqslant T_{As}$ and $\zeta^+ = 0$ at $T = T_{Af}$. Similarly, upon cooling from T_f,

$$\varepsilon_f(T) = \sigma_f/E_f(T) + \alpha_f(T - T_f) + \varepsilon_T\zeta^-(T), \tag{25b}$$

where ζ^- is the fraction of the martensite phase during cooling, with $\zeta^- = 0$ for $T \geqslant T_{\mathrm{Ms}}$ and $\zeta^- = 1$ at $T = T_{\mathrm{Mf}}$. For SMAs, both α_{f} and the recoverable strain ε_{T} can be taken as temperature independent. However, E_{f} depends on temperature, because $E_{\mathrm{A}} \approx 3E_{\mathrm{M}}$. For heating

$$E_{\mathrm{f}}(T) = E_{\mathrm{M}} + \zeta^+(T)(E_{\mathrm{A}} - E_{\mathrm{M}}) \tag{26}$$

and, for cooling

$$E_{\mathrm{f}}(T) = E_{\mathrm{A}} + \zeta^-(T)(E_{\mathrm{M}} - E_{\mathrm{A}}). \tag{27}$$

Since the martensite fraction calculated using the transformation free-energy driving force (Tanaka, 1986) does not give a realistic representation (Zhang et al., 1997), the following phenomenological relation (Liang and Rogers, 1990) has been chosen. For heating

$$\zeta^+ = \frac{1}{2}\left\{\cos\pi\left(\frac{T - T_{\mathrm{As}}}{T_{\mathrm{Af}} - T_{\mathrm{As}}} - \frac{|\sigma_{\mathrm{f}}|}{c_{\mathrm{A}}(T_{\mathrm{Af}} - T_{\mathrm{As}})}\right)^{n^+} + 1\right\} \tag{28a}$$

and, for cooling,

$$\zeta^- = \frac{1}{2}\left\{\cos\pi\left(\frac{T - T_{\mathrm{Mf}}}{T_{\mathrm{Ms}} - T_{\mathrm{Mf}}} - \frac{|\sigma_{\mathrm{f}}|}{c_{\mathrm{M}}(T_{\mathrm{Ms}} - T_{\mathrm{Mf}})}\right)^{n^-} + 1\right\}. \tag{28b}$$

Here c_{A} and c_{M} are the slopes of the stress versus transition temperature curves (Fig. 8a). Experimental evidences suggest that $c_{\mathrm{A}} \approx c_{\mathrm{M}}$, and that the influence of

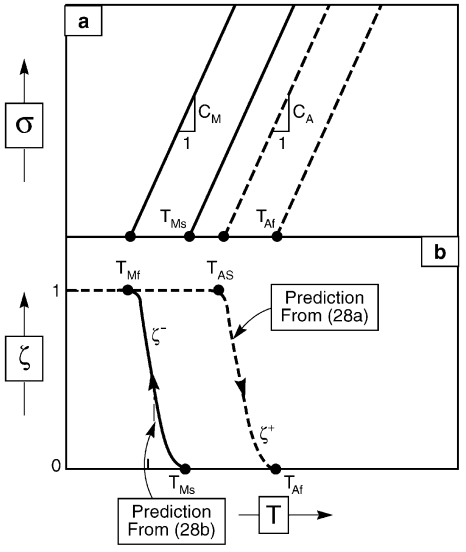

Fig. 8. (a) Effect of applied stress on transformation temperatures; (b) evolution of martensite fraction with temperature.

applied stress on the phase transformation is nearly linear, consistent with the Clausius–Clapeyron relation (Zhang et al., 1997). For NiTi SMAs, $c_A \approx c_B \approx 10\,\text{MPa/K}$. The exponents n^+ and n^- are introduced to fit the experimental curve ($n^+ = n^- \approx 1$ is normally expected). The martensite fraction predicted from Eq. (28) is schematically shown in Fig. 8b.

3.6. End deflection

Upon heating, the length of the top face is reduced by, $\Delta L = -\varepsilon_f L$, where ε_f is given by Eq. (25a). The small constraining effect due to the triangular corrugated core has been ignored. The bottom face does not stretch nor contract, causing the beam to bend upwards as illustrated in Fig. 1c. (The downward flexure initiates when the power to the top face is switched off and that for the bottom face is turned on.) The tip deflection due to the combined effect of shape memory contraction and thermal expansion, δ_1, is

$$\delta_1 = H\left(\frac{1}{2} + \frac{L}{\Delta L}\right)\left(1 - \cos\frac{\Delta L}{H}\right). \tag{29}$$

If $\Delta L/2L \ll 1$ (which is valid under most situations) and $\Delta L/H < 1/2$ (i.e. $L/H < 10$ for $\varepsilon^T \approx 0.05$, which may be unduly constrained), Eq. (29) simplifies to

$$\delta_1 \approx -\frac{\varepsilon_f L^2}{2H}. \tag{30a}$$

The tip deflection δ_2 due to a resistance N imposed at the free end is (Allen, 1969)

$$\frac{\delta_2}{N/E_f B} = \frac{2}{3}\frac{L^3}{dH^2} + \frac{3\sqrt{3}}{2}\frac{E_f}{E_c}\frac{L}{d_c}. \tag{30b}$$

Accordingly, the tip deflection, $\delta = \delta_1 - \delta_2$, can be calculated for the full operational cycle. As previously stated, when the transformation is complete, the cantilever is required to deflect at the end by at least δ_0. The deflection constraint for the actuator is then given by

$$\delta_f = \frac{H}{\varepsilon_T - \alpha_f \Delta T_f}\left(1 - \cos\frac{\varepsilon_T - \alpha_f \Delta T_f}{H/L}\right) - \frac{N}{E_A B}\left(\frac{2}{3}\frac{L^3}{dH^2} + \frac{3\sqrt{3}}{2}\frac{E_A}{E_c}\frac{L}{d_c}\right) \geqslant \delta_0, \tag{31}$$

where $E_A = E_f(T_{Af})$. For $(\varepsilon_T - \alpha_f \Delta T_f)L/H < 1/2$, (31) simplifies to

$$\delta_f = \frac{(\varepsilon_T - \alpha_f \Delta T_f)L^2}{2H} - \frac{N}{E_A B}\left(\frac{2}{3}\frac{L^3}{dH^2} + \frac{3\sqrt{3}}{2}\frac{E_A}{E_c}\frac{L}{d_c}\right) \geqslant \delta_0. \tag{32}$$

For preliminary screening, H may be chosen such that δ_f is maximized at specified L. For example, maximizing δ_f against H results in

$$\frac{H}{L} = \frac{8}{3}\frac{N/Bd}{E_A(\varepsilon_T - \alpha_f \Delta T_f)}. \tag{33}$$

3.7. Failure criteria

Mechanical failure, if it occurs, is caused by the member stresses arising from the induced force N. Because $E_A \approx 3E_M$ and the yield strength of the NiTi alloy is approximately constant (Otsuka and Wayman, 1998), it is expected that such failure would occur at low temperatures when the SMA is 100% martensite. For the system with the polymer core, four different types of failure are considered: face yielding, face buckling, core yielding and core buckling. Yielding will be avoided if

$$\sigma_f \leqslant \sigma_Y^f \quad \text{(face yielding)}, \tag{34a}$$

$$\sigma_c \leqslant \sigma_Y^c \quad \text{(core yielding)} \tag{34b}$$

and local buckling will be averted if

$$\sigma_f \leqslant \frac{\chi_f \pi^2 E_M}{48}\left(\frac{d}{\lambda}\right)^2 \quad \text{(face buckling)}, \tag{35a}$$

$$\sigma_c \leqslant \frac{\chi_c \pi^2 E_c}{18}\left(\frac{d_c}{H}\right)^2 \quad \text{(core buckling)}, \tag{35b}$$

where $\chi_f = \chi_c = 1$ for members simply supported at the ends and $\chi_f = \chi_c = 4$ for members fully clamped at the ends (Allen and Bulson, 1980). The choice $\chi_f = \chi_c = 1$ neglects the rotational resistance at the joints and underestimates the critical load associated with local buckling, whereas the choice $\chi_f = \chi_c = 4$ overestimates the critical load. To address actual behavior, the common practice used in structural design (Tall, 1974; Wiernicki et al., 1991) is adopted. Constraints (35) now become

$$\sigma_f \leqslant \frac{\pi^2 E_M}{48}\left(\frac{d}{K_f \lambda}\right)^2 \quad \text{(face buckling)}, \tag{36}$$

$$\sigma_c \leqslant \frac{\pi^2 E_c}{18}\left(\frac{d_c}{K_c H}\right)^2 \quad \text{(core buckling)}, \tag{37}$$

where K_f and K_c are effective length factors given by

$$K_f = \frac{\pi^2 + 2/N_f}{\pi^2 + 4/N_f}, \quad K_c = \frac{\pi^2 + 2/N_c}{\pi^2 + 4/N_c} \tag{38}$$

with

$$N_f = \frac{E_M I_f}{2\lambda}\left(\frac{1}{\bar{R}_f}\right), \quad N_c = \frac{E_c I_c}{\sqrt{2}H}\left(\frac{1}{\bar{R}_c}\right). \tag{39}$$

Here, $I_f = d^3/12$, $I_c = d_c^3/12$, $\bar{R}_f$ is the rotational stiffness at the ends of the face member and $\bar{R}_c$ is the rotational stiffness at the ends of the core member, given by

$$\bar{R}_f = \frac{E_M d^3}{8H} + \frac{E_c d_c^3}{2\sqrt{2}H}, \quad \bar{R}_c = \frac{E_M d^3}{4H} + \frac{E_c d_c^3}{4\sqrt{2}H}. \tag{40}$$

By comparing Eqs. (35) with (37), it follows that

$$\chi_f = 1/K_f^2, \quad \chi_c = 1/K_c^2. \tag{41}$$

Note that if $\bar{R}_f = \bar{R}_c \to \infty$, $K_f = K_c = 0.5$, so that the case of fully clamped ends ($\chi_f = \chi_c = 4$) is recovered. When the other limiting case ($\bar{R}_f = \bar{R}_c = 0$) prevails, $K_f = K_c = 1$ and the condition of simply supported ends ($\chi_f = \chi_c = 1$) is in place. In general, for triangular corrugated core sandwiches, $0.5 \leqslant K_f \leqslant 1$ and $0.5 \leqslant K_c \leqslant 1$.

For the Si system, core yielding is not a failure mode. It is replaced by brittle fracture, which happens when the tensile stress attains the fracture strength, σ_0^c: whereupon, (34b) is replaced by: $\sigma_c \leqslant \sigma_0^c$.

4. Lowest weight and power

4.1. Formulation of the optimization problem

The nonlinear optimization problem for minimum weight can be summarized using non-dimensional variables. The initial goal is to minimize the actuator weight given in non-dimensional form by

$$\Psi \equiv \frac{W}{\rho_f BL^2} = 2\frac{d}{L} + \sqrt{3}\frac{\rho_c}{\rho_f}\frac{d_c}{L} \tag{42}$$

subject to the following six constraints

$$1 - \frac{L/\delta_0}{\varepsilon_T - \alpha_f \Delta T_f}\frac{H}{L}\left(1 - \cos\frac{\varepsilon_T - \alpha_f \Delta T_f}{H/L}\right) + \frac{N}{E_A BL}\frac{L}{\delta_0} \times \left\{\frac{2}{3}\frac{L}{d}\left(\frac{L}{H}\right)^2 + \frac{3\sqrt{3}}{2}\frac{E_A}{E_c}\frac{L}{d_c}\right\} \leqslant 0 \quad \text{(minimum deflection)}, \tag{43a}$$

$$2\frac{BLh\Delta T_f}{P_0}\{1 - e^{-2(L/d)(ht^+/\rho_f c_p^f L)}\}^{-1} - 1 \leqslant 0 \quad \text{(power consumption)}, \tag{43b}$$

$$\frac{N}{E_A BL}\frac{E_A}{\sigma_Y^f}\frac{L}{d}\frac{L}{H} - 1 \leqslant 0 \quad \text{(face yielding)}, \tag{43c}$$

$$\frac{\sqrt{6}}{2}\frac{N}{E_A BL}\frac{E_A}{\sigma_Y^c}\frac{L}{d_c} - 1 \leqslant 0 \quad \text{(core member yielding)} \tag{43d}$$

with σ_Y^c replaced by σ_0^c for Si cores

$$\frac{72}{\pi^2}\frac{N}{E_A BL}\frac{H}{L}\left(\frac{L}{d}\right)^3\left(\frac{\pi^2 + 2/N_f}{\pi^2 + 4/N_f}\right)^2 - 1 \leqslant 0 \quad \text{(face buckling)}, \tag{43e}$$

$$\frac{9\sqrt{6}}{\pi^2}\frac{N}{E_A BL}\frac{E_A}{E_c}\left(\frac{H}{L}\right)^2\left(\frac{L}{d_c}\right)^3\left(\frac{\pi^2 + 2/N_c}{\pi^2 + 4/N_c}\right)^2 - 1 \leqslant 0 \quad \text{(core member buckling)}, \tag{43f}$$

where

$$N_{\mathrm{f}} = \frac{1}{3}\left\{1 + \frac{9\sqrt{2}}{2}\frac{E_{\mathrm{c}}}{E_{\mathrm{A}}}\left(\frac{d_{\mathrm{c}}}{L}\frac{L}{d}\right)^3\right\}^{-1}, \quad N_{\mathrm{c}} = \frac{1}{3}\left\{1 + \frac{\sqrt{2}}{3}\frac{E_{\mathrm{A}}}{E_{\mathrm{c}}}\left(\frac{d}{L}\frac{L}{d_{\mathrm{c}}}\right)^3\right\}^{-1}.$$

If the actuator needs to be designed to operate above a specified frequency f_0, then it must also satisfy

$$\frac{f_0\rho_{\mathrm{f}}c_p^{\mathrm{f}}L}{2h}\frac{d}{L}\left\{6 - \ln\left(1 - \frac{2BLh\Delta T_{\mathrm{f}}}{P_0}\right)\right\} - 1 \leqslant 0 \quad \text{(minimum frequency)}. \tag{43g}$$

With the assumption that $H = 2\sqrt{\lambda}$, it is seen from Eq. (42) that the dimensionless weight of the actuator depends only on two geometrical variables, d/L and d_{c}/L. The other geometrical variable, H/L, is a solution to the optimization. The remaining dimensionless load, material, displacement, electrical, transformation, time and frequency variables appearing in the optimization are all specified, and are grouped together as follows:

$$\textit{Load index} : \Pi \equiv \frac{N}{E_{\mathrm{A}}BL},$$

$$\textit{Power index} : \frac{P_0}{k_{\mathrm{f}}L\Delta T_{\mathrm{f}}},$$

$$\textit{Time index} : \frac{k_{\mathrm{f}}t^+}{\rho_{\mathrm{f}}c_p^{\mathrm{f}}BL},$$

$$\textit{Frequency index} : \frac{f_0\rho_{\mathrm{f}}c_p^{\mathrm{f}}BL}{k_{\mathrm{f}}}$$

and the strains are: $\varepsilon_{\mathrm{T}} - \alpha_{\mathrm{f}}\Delta T_{\mathrm{f}}$, $\varepsilon_{\mathrm{Y}}^{\mathrm{c}} \equiv \sigma_{\mathrm{Y}}^{\mathrm{c}}/E_{\mathrm{A}}$, $\varepsilon_{\mathrm{Y}}^{\mathrm{f}} \equiv \sigma_{\mathrm{Y}}^{\mathrm{f}}/E_{\mathrm{A}}, \delta_0/L$.

4.2. Illustrative example

The graphical method for optimization introduced by Gibson and Ashby (1997) for sandwich panels is used, complimented by the sequential quadratic programming method with the IMSL software. The design variables are d/L, d_{c}/L and H/L; the rest of the parameters are specified (Table 2). A typical example (Fig. 9), which uses d/L and H/L as co-ordinates, is plotted for fixed restraining force ($N = 10\mathrm{N}$) and one choice of d_{c}/L (5×10^{-3}). The acceptable range of d/L and H/L is represented by the shaded region. Since the weight is independent of H/L, the lowest weight is represented by smallest d/L. This occurs at the intersection site C. Moreover, site C represents the design that operates at lowest power, thereby simultaneously satisfying two of the goals. That this design also satisfies the core buckling constraint is verified from the curve representing (43f). Furthermore, although core yielding does not appear in the figure, it must be verified that this criterion is satisfied by substituting the parameters from Table 2 into Eq. (43d).

By evaluating this intersection for a range of parameters (and checking on the structural integrity in each case), a locus of conditions that simultaneously give low weight

Table 2
Parameters used to generate deflection maps

SMA faces
$E_A = 90\,\text{GPa}$
$\sigma_Y^f = 200\,\text{MPa}$
$\alpha_f = 10^{-5}\,\text{K}^{-1}$
$\varepsilon_T = 0.05$
$\rho_f = 6500\,\text{kg/m}^3$

Polymer core
$E_c = 2\,\text{GPa}$
$\sigma_Y^c = 40\,\text{MPa}$
$\rho_c = 1300\,\text{kg/m}^3$

Si *core*
$E_c = 170\,\text{GPa}$
$\sigma_Y^c = 600\,\text{MPa}$
$\rho_c = 2200\,\text{kg/m}^3$

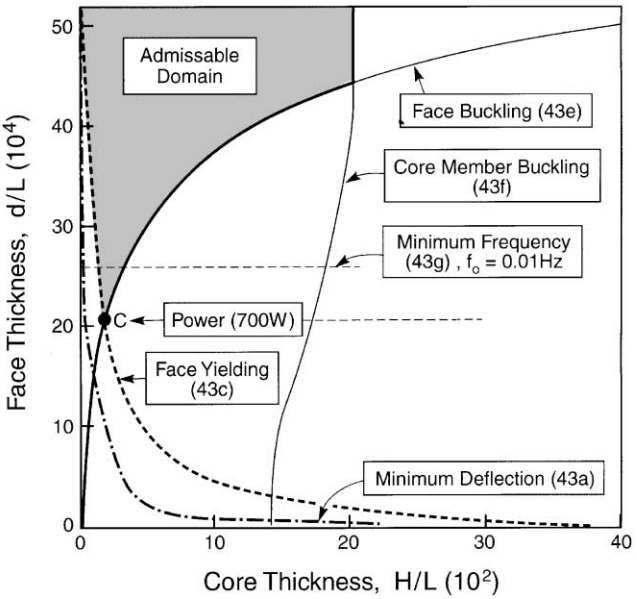

Fig. 9. Selection map for acceptable dimensions subjected to the constraints (43), with $N = 10\,N$ and $d_c/L = 5\times10^{-3}$. The rest of parameters used are listed in Table 2.

and low power can be constructed. The results are plotted in Figs. 10–12. The lowest weight, $\Psi_{\min}$ and the associated dimensions (d/L, d_c/L and H/L) are determined as a function of the load index (Fig. 10). Both polymer and silicon cores are used. For a specified load index, actuators made with the stiffer and stronger silicon core

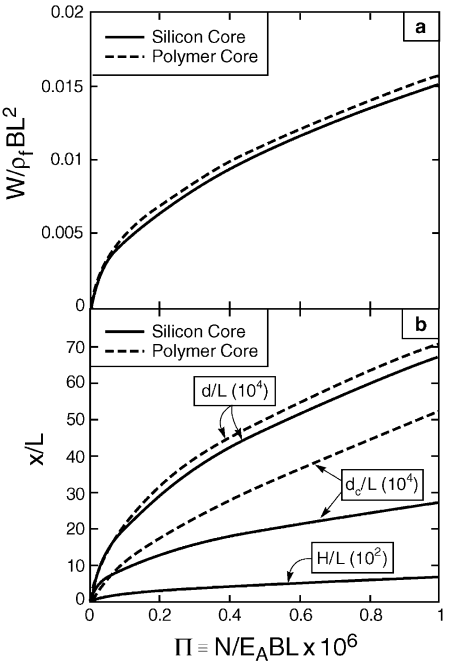

Fig. 10. (a) Minimum weight and (b) the associated dimensions plotted as functions of load index Π.

weigh (slightly) less than those having a polymer core (Fig. 10a), whereas the minimal thickness of the silicon core member d_c is reduced by about a factor of two (Fig. 10b). However, the results for the Si core could be optimistic because the thermal conductance of the Si has not been taken into account.

The lowest power and the highest operating frequency are linked by Eq. (18): both depend on the optimized face thickness as well as the heat transfer coefficient. The non-dimensional results displayed in Fig. 11 are applicable for both polymer and silicon cores (because power and frequency are not sensitive to variation in core properties), with the Biot number being either 0.01 or 0.5, corresponding to $h = 20\,\mathrm{W/m^2K}$ (natural air convection) and $1000\,\mathrm{W/m^2K}$ (water cooling). Note that, while the power requirement increases as the load index increases, the frequency decreases (Fig. 11). One consequence is that, for small mechanical devices (micron-to-millimeter) that operate at relatively low loads, small Π, natural air convection permits high frequency at low power (Krulevitch et al., 1996). To provide a more definite sense about requirements, the results for two point designs are presented in Fig. 12: one for a small actuator and the other for a large actuator.

4.3. Comparison with shape memory bimorph

To demonstrate the advantages of the present corrugated design, the preceding results are compared with those for a conventional bimorph actuator. The non-dimensional

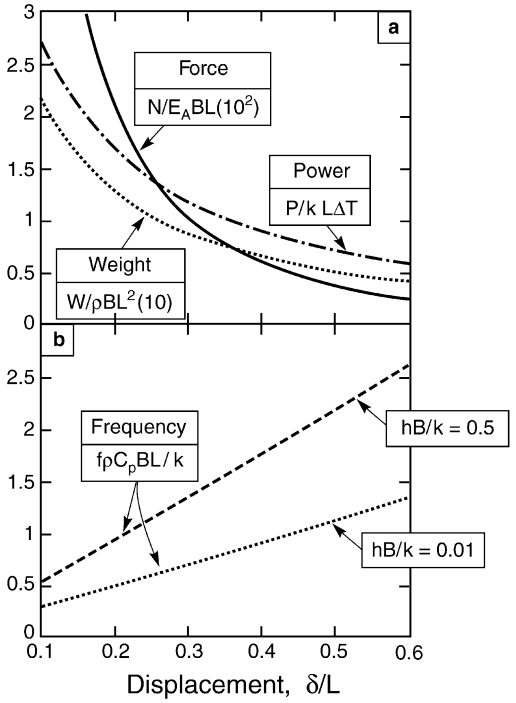

Fig. 11. Variations in non-dimensional indices with specified end deflection: (a) force, weight and power (these are independent of the Biot number); (b) the frequency for two representative values of Biot number.

weight of a bimorph cantilever can be expressed as

$$\frac{W}{\rho_f BL^2} = \frac{d}{L} + \frac{\rho_s}{\rho_f}\frac{d_s}{L}, \tag{44}$$

where the subscript "s" is used to denote parameters associated with the substrate. The rest of the parameters are given in Fig. 1. The tip deflection when heated from T_0 to T_{Af} is

$$\frac{\delta_f}{L} = \frac{L}{2R} - \frac{NL^2}{3(EI)_{eq}}, \tag{45}$$

where R is the radius of curvature of the bimorph (Timoshenko, 1925)

$$\frac{1}{R} = \frac{\varepsilon_T - \Delta\alpha\Delta T}{D/2 + 2(EI)_{eq}/D(1/E_A d + 1/E_s d_s)}. \tag{46}$$

In Eq. (46), $\Delta\alpha = \alpha_f - \alpha_s$, $\Delta T = T_{Af} - T_0$, and $D = d + d_s$. The maximum stress in the SMA layer is

$$\sigma_f = \frac{1}{R}\left(\frac{2(EI)_{eq}}{Dd} + \frac{E_A d}{2}\right) + \frac{NLD}{2BI_{eq}}, \tag{47}$$

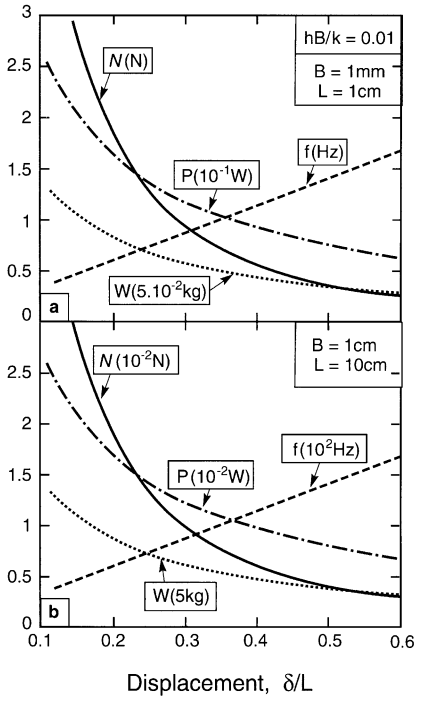

Fig. 12. Actual values of power, load, weight and frequency for two point designs.

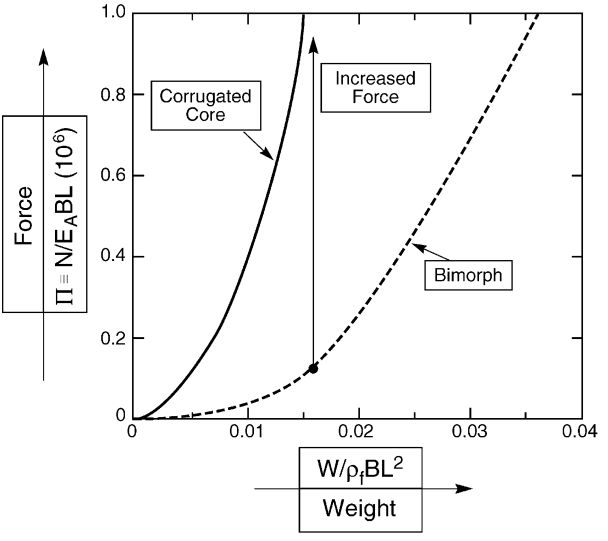

Fig. 13. Minimum weight plotted as functions of load index Π for NiTi/Si corrugated beam and bimorph. Note the substantially larger force that can be displaced by the new design for the same actuator weight.

where I_{eq} is the moment of inertia of the bimorph cross-section. A related expression can be derived for the maximum stress in the substrate. To determine $(EI)_{eq}$ and I_{eq}, the bimorph may be treated as homogeneous (effective modulus, $E=(E_A+E_s)/2$), with an error typically less than 10% (Timoshenko, 1925).

The minimum weight and the associated optimal dimensions of the bimorph have been calculated subject to the following constraints: minimum deflection, SMA film yielding, substrate cracking, and buckling. The results are obtained for the SMA/silicon system (Fig. 13) and compared with those for beams with triangular cores. Note that when the load index, $\Pi > 2\times10^{-7}$, the failure mode switches from buckling to film yielding; substrate cracking is not active for the range of load index investigated. When optimized, the performance of the corrugated design substantially exceeds that for the bimorph, since the curves are highly non-linear. Note from Fig. 13 that when the weight or thickness of the actuator are specified, the forces that can be displaced are considerably larger for the new design. At low weight and small dimensions, this advantage can be in excess of an order of magnitude. Moreover, since the temperature history of the SMA film is about the same in both designs (silicon being a good thermal conductor), the power consumed by the bimorph exceeds that needed by a corrugated beam and its operational frequency is significantly lower.

5. Conclusion

It has been shown that cantilever actuators consisting of SMA face sheets and triangular corrugated cores can be designed to operate against large restraining moments at relatively low weight relative to competing concepts, such as bimorphs. The triangular corrugation is attractive owing to its minimal rotational/bending resistance and high transverse shear stiffness: whereupon the core remains unstressed as the face sheets contract due to phase transformation. Polymer and silicon cores have both been considered: the former suitable for actuators in the size range 1 mm $\rightarrow$ 1 m, and the latter for miniature actuators ($\leqslant$1 mm). The minimum power usage and maximum operational frequency that can be achieved have been calculated, both as functions of the load index.

Acknowledgements

This work is supported partially by the DAPRA/ONR MURI program on Ultralight Metal Structures, USA (No. N00014-1-96-1028) and partially by the EPSRC, UK. The authors are indebted to Nathaniel Wicks for help on solving the nonlinearly constrained minimization problem by using the sequential quadratic programming method with the IMSL software.

References

Allen, H.G., 1969. Analysis and Design of Structural Sandwich Panels. Pergamon Press, Oxford.
Allen, H.G., Bulson, P.S., 1980. Background to Buckling. McGraw-Hill Ltd., London.

Ataka, M., Omodaka, A., Takeshima, N., Fujita, H., 1993. Fabrication and operation of polymide bimorph actuators for a ciliary motion system. J. Microelectromech. Systems 2, 146–150.

Budiansky, B., 1999. On the minimum weights of compression structures. Int. J. Solids Struct. 36, 3677–3708.

Carslaw, H.S., Jaeger, J.C., 1959. Conduction of Heat in Solids. Oxford University Press, Oxford.

Gibson, L.J., Ashby, M.F., 1997. Cellular Solids: Structure and Properties: 2nd Edition. Cambridge University Press, Cambridge.

Gu, S., Lu, T.J., Evans, A.G., 2001. On the design of two-dimensional cellular metals for combined heat dissipation and structural load capacity. Int. J. Heat Mass Transfer, in press.

Jegley, D.C., 1992. A study of compression-loaded and impact-damaged structurally efficient graphite-thermoplastic trapezoidal-corrugation sandwich and semi-sandwich panels. NASA TP-3269.

Kato, H., Stalmans, R., Van Humbeeck, J., 1998. Two-way shape memory effect induced by tension training in Cu-13.4Al-4.0Ni (mass%) alloy single crystals. Mater. Tran., JIM 39, 378–386.

Krulevitch, P., Lee, A.P., Ramsey, P.B., Trevino, J.C., Hamilton, J., Northrup, M.A., 1996. Thin film shape memory alloy microactuators. J. Microelectromech. Systems 5, 270–281.

Liang, C., Rogers, C.A., 1990. One-dimensional thermomechanical constitutive relations for shape memory materials. J. Intell. Mater. Systems Struct. 1, 207–234.

Lin, L., Lin, S.-H., 1998. Vertically driven microactuators by electrothermal buckling effects. Sensors and Actuators A71, 35–39.

Lu, T.J., 1999. Heat transfer efficiency of metal honeycombs. Int. J. Heat Mass Transfer 42, 2031–2040.

Lu, T.J., Chen, C., Zhu, G., 2001. Compressive behavior of corrugated board panels. J. Comp. Mater., in press.

Makino, E., Mitsuya, T., Shibata, T., 2000. Dynamic actuation properties of TiNi shape memory diaphragm. Sensors and Actuators A79, 128–135.

Otsuka, K., Wayman, C.M., 1998. Shape Memory Materials. Cambridge University Press, Cambridge, UK.

Peirs, J., Reynaerts, D., Van Brussel, H., 1998. Design of a shape memory actuated endoscopic tip. Sensors and Actuators A70, 135–140.

Tall, L., 1974. Structural Steel Design, 2nd Edition. The Ronald Press Co., New York.

Timoshenko, S., 1925. Analysis of bi-metal thermostats. J. Opt. Soc. Am. 11, 233–255.

Webb, G., Wilson, L., Lagoudas, D., Redinotis, O., 2000. Adaptive control of shape memory alloy actuators for underwater biomimetic applications. AIAA J. 38, 325–334.

Wicks, N., Hutchinson, J.W., 2000. Optimal truss plates. Harvard University, Division of Engineering and Applied Sciences Report, Mech-362.

Wiernicki, C.J., Liem, P.E., Woods, G.D., Furio, A.J., 1991. Structural analysis methods for lightweight metallic corrugated core sandwich panels subjected to blast loads. Naval Eng. J. 103, 192–203.

Zhang, J.X., Liu, Y.X., Cai, W., Zhao, L.C., 1997. The mechanisms of two-way shape memory effect in a Cu–Zn–Al alloy. Mater. Lett. 33, 211–214.